He II λ4686 IN η CARINAE: COLLAPSE OF THE WIND–WIND COLLISION REGION DURING PERIASTRON PASSAGE

M. Teodoro[1], A. Damineli[1], J. I. Arias[2], F. X. de Araújo[3,16], R. H. Barbá[4,17], M. F. Corcoran[5,18], M. Borges Fernandes[3],
E. Fernández-Lajús[6,19], L. Fraga[7], R. C. Gamen[6,19], J. F. González[4], J. H. Groh[8], J. L. Marshall[9], P. J. McGregor[10],
N. Morrell[11], D. C. Nicholls[10], E. R. Parkin[10], C. B. Pereira[3], M. M. Phillips[11], G. R. Solivella[6,19], J. E. Steiner[1],
M. Stritzinger[12,20], I. Thompson[13], C. A. O. Torres[14], M. A. P. Torres[15,21], and M. I. Zevallos Herencia[3]

[1] Instituto de Astronomia, Geofísica e Ciências Atmosféricas, Universidade de São Paulo, Rua do Matão 1226,
Cidade Universitária, São Paulo 05508-900, Brazil; mairan@astro.iag.usp.br
[2] Departamento de Física, Universidad de La Serena, Av. Cisternas 1200 Norte, La Serena, Chile
[3] Observatório Nacional, Rua General José Cristino 77, São Cristóvão, Rio de Janeiro 20921-400, Brazil
[4] Instituto de Ciencias Astronómicas, de la Tierra, y del Espacio (ICATE-CONICET), Avenida España Sur 1512, J5402DSP San Juan, Argentina
[5] CRESST and X-ray Astrophysics Laboratory, NASA/Goddard Space Flight Center, Greenbelt, MD 20771, USA
[6] Facultad de Ciencias Astronómicas y Geofísicas, Universidad Nacional de La Plata, Paseo del Bosque s/n, La Plata, BA, B1900FWA, Argentina
[7] Southern Observatory for Astrophysical Research, Colina El Pino s/n, Casilla 603, La Serena, Chile
[8] Max-Planck-Institute für Radioastronomie, Auf dem Hügel 69, D-53121 Bonn, Germany
[9] Department of Physics and Astronomy, Texas A&M University, College Station, TX 77843-4242, USA
[10] Research School of Astronomy and Astrophysics (RSAA), Mount Stromlo Observatory, Cotter Road, Weston, ACT 2611, Australia
[11] Las Campanas Observatory, Observatories of the Carnegie Institution of Washington, Casilla 601, La Serena, Chile
[12] The Oskar Klein Centre, Department of Astronomy, Stockholm University, AlbaNova, 10691 Stockholm, Sweden
[13] Observatories of the Carnegie Institution, 813 Santa Barbara Street, Pasadena, CA 91101, USA
[14] Laboratório Nacional de Astrofísica, Rua Estados Unidos 154, Bairro das Nações, 37504-364 Itajubá, Brazil
[15] Harvard-Smithsonian Center for Astrophysics, 60 Garden Street, Cambridge, MA 02138, USA

ABSTRACT

The periodic spectroscopic events in η Carinae are now well established and occur near the periastron passage of two massive stars in a very eccentric orbit. Several mechanisms have been proposed to explain the variations of different spectral features, such as an eclipse by the wind–wind collision (WWC) boundary, a shell ejection from the primary star or accretion of its wind onto the secondary. All of them have problems explaining all the observed phenomena. To better understand the nature of the cyclic events, we performed a dense monitoring of η Carinae with five Southern telescopes during the 2009 low-excitation event, resulting in a set of data of unprecedented quality and sampling. The intrinsic luminosity of the He II λ4686 emission line ($L \sim 310\,L_\odot$) just before periastron reveals the presence of a very luminous transient source of extreme UV radiation emitted in the WWC region. Clumps in the primary's wind probably explain the flare-like behavior of both the X-ray and He II λ4686 light curves. After a short-lived minimum, He II λ4686 emission rises again to a new maximum, when X-rays are still absent or very weak. We interpret this as a collapse of the WWC onto the "surface" of the secondary star, switching off the hard X-ray source and diminishing the WWC shock cone. The recovery from this state is controlled by the momentum balance between the secondary's wind and the clumps in the primary's wind.

Key words: line: profiles – stars: early-type – stars: individual (eta Carinae) – stars: massive

Online-only material: color figures

1. INTRODUCTION

The stellar object η Carinae (HD 93308; hereafter η Car) is one of the most luminous and massive of our Galaxy. Since its "Great Eruption" in 1843 (Smith & Frew 2011), it has been frequently observed at a variety of wavelengths. This object has a central source enshrouded by thick ejecta, which, on one hand, precludes a clear view of the central engine, but, on the other hand, displays dynamical and chemical indications of a probable hypernova progenitor (Paczynski 1998; Smith et al. 2007).

The spectrum of η Car is rich in low-excitation forbidden and permitted lines (Thackeray 1953), as well as high-excitation forbidden ones (Damineli et al. 1998, and references therein), which temporarily disappeared in 1948, and again in 1965, 1981, 1987, and 1992. These "spectroscopic events" (Gaviola 1953; Rodgers & Searle 1967; Thackeray 1967; Zanella et al. 1984) or "low-excitation events" (Damineli et al. 1998) were originally believed to be part of S Doradus cycles, commonly seen in other luminous blue variable (LBV) stars similar to η Car. This interpretation seemed to be supported by the observations of the He I λ10830 line, which reached minimum (Damineli 1996) close to the maximum of the near-infrared light curve (Whitelock et al. 1994). However, the spectroscopic events were demonstrated to be strictly periodic (Damineli et al. 2000), in contrast to the incoherent variations characteristic of S Doradus oscillations.

Periodic minima are in fact observed throughout the electromagnetic spectrum—in doubly ionized forbidden, permitted, and UV pumped lines in the optical and UV bands; in

---

near-infrared continuum flux; in X-ray flux; and in mm and cm radio flux. The presence of a binary system (Damineli et al. 1997) accounts for the strict periodicity of these minima (Corcoran 2005; Fernandez Lajus et al. 2010; Damineli et al. 2008b). In the binary scenario, the primary star is the most luminous member of the system. It is moderately evolved (in the LBV phase) and has a slow ($\sim$500 km s^{-1}) and dense wind in which the low-excitation lines are formed (Hillier et al. 2001, 2006). The companion star is not detected in the spectrum, being less luminous, less massive, hotter, and with a fast ($\sim$3000 km s^{-1}) wind (Corcoran 2005). The orbit is very eccentric and may even be higher than $e = 0.9$. At apastron, the secondary star would be placed on our side of the primary, since the Weigelt blobs—which are circumstellar material located $\sim$0.3 arcsec from the central source at our side of the system (Weigelt & Ebersberger 1986; Weigelt et al. 1995)—display a high-excitation state during most of the orbital cycle (Davidson et al. 1997; Dorland et al. 2004; Smith et al. 2004). The high-excitation forbidden lines are absent from the spectrum for a relatively brief time ($\sim$6 months) when the system is close to periastron (Damineli et al. 2008a). Moreover, X-ray observations indicate that the column density (N_H) is lower toward apastron (Hamaguchi et al. 2007), indicating that the WWC shock cone is opened toward our direction at those phases. However, some authors have suggested different system orientations (Abraham et al. 2005; Soker 2005; Kashi & Soker 2008; Falceta-Gonçalves & Abraham 2009). Nevertheless, the binary scenario has gained support from many analyses (Ishibashi et al. 1999; Pittard & Corcoran 2002; Okazaki et al. 2008; Parkin et al. 2009, 2011).

The suggestion of a wind–wind collision (hereafter WWC; Damineli et al. 1997; Damineli 1997) explains the excess X-ray emission as compared to other binaries containing hot luminous components, especially at energies greater than 2 keV. Ishibashi et al. (1999), using the analytical model of Usov (1992), were able to account for the main features in the X-ray emission and for the general behavior of the X-ray light curve, in particular, the increase in the X-ray flux just before periastron. They attributed the rapid drop in X-ray flux at periastron to an increase in the column density (N_H) of the intervening gas from the primary star in the line of sight, as the secondary star moved behind the primary. The duration of the X-ray minimum, however, was too long compared to the predictions of the analytical model, and an ad hoc disk around the equator of the primary star was suggested as an additional source of obscuration (Ishibashi et al. 1999). However, Damineli et al. (1999) noted that an eclipse could not produce simultaneously a minimum in X-rays and in the high-excitation lines, which are located at different distances and directions relative to our line of sight, but which disappear at nearly the same time.

Alternative models assumed transient phenomena around periastron to explain the disappearance of X-rays—e.g., shell ejection (Davidson et al. 2005), accretion onto the secondary companion (Soker 2003, 2005, 2007; Soker & Behar 2006), but all of them face problems when confronted with the whole set of observational data. This is due to the fact that the spectroscopic cycle (i.e., the time interval between two consecutive disappearances of doubly ionized lines or narrow components in He I lines) has two components: a "slow variation" and a "collapse" (Damineli et al. 2008a). Each component affects the cycle in a different way. The "slow variation" component is seen along the whole spectroscopic cycle as a smooth periodic modulation in the radio emission and in the intensity of low-excitation spectral features (e.g., singly ionized lines and the near-infrared

emission). The minimum of the "slow variation" component is centered at $\phi \sim 0.07$.[22] The "collapse" component regulates the intensity of the high-energy features (e.g., X-rays, doubly ionized lines) with a minimum centered at $\phi \sim 0.03$. Since the spectroscopic cycle is composed of these two components, any short-lived mechanism (shell ejection, accretion, etc.) invoked to explain the "collapse" would not be able to also explain the "slow variation" component.

Modeling the WWC seems to be a viable option to derive the orbital parameters. Many models to explain the physics of the WWC have been presented, including two-dimensional and three-dimensional (3D) numerical simulations (Pittard & Corcoran 2002; Okazaki et al. 2008; Parkin et al. 2009, 2011). For reference, Figure 1 shows the WWC from a 3D model (Parkin et al. 2011) in which we have identified the main regions and structures discussed in the following sections. Groh et al. (2010) showed that a 3D numerical smoothed-particle hydrodynamics model (Okazaki et al. 2008) could successfully explain the high-velocity absorption component ($v \gtrsim 2000$ km s^{-1}) seen in He I λ10830 near periastron. This high-velocity feature requires a large column density of high-velocity gas in the line of sight, and they derived a periastron longitude $\omega = 240°$–$270°$ (consistent with an orientation such that the companion is on the near side of the primary at apastron) and orbital inclination $i = 40°$–$60°$. The He I λ10830 line is emitted close to the WWC apex, which revolves very rapidly at periastron. Modeling of the spatially resolved forbidden line emission led to a similar longitude of periastron (Gull et al. 2009, 2011; Madura et al. 2011).

In η Car, the detection of He II λ4686 emission (Steiner & Damineli 2004) provided a new tool with which to study the WWC (Martin et al. 2006; Soker & Behar 2006; Abraham & Falceta-Gonçalves 2007). Steiner & Damineli (2004) found that this emission is present throughout the entire 5.538 yr cycle, but at a low-intensity level (equivalent width, $|EW| < 0.1$ Å) for most of the orbit. The intensity of the line rises suddenly by one order of magnitude near $\phi = 0$ and then sharply decreases to zero, after which the intensity reaches a lower peak and then declines. The intrinsic luminosity emitted in this spectral line (after correction for interstellar and circumstellar extinction) is greater than the maximum unabsorbed X-ray luminosity in the 2–10 keV band ($\sim$67 $L_\odot$; Ishibashi et al. 1999). An ultraviolet source with $\sim$10^4 $L_\odot$ at energies higher than the He$^+$ ionization limit (54.4 eV) is needed to populate the upper level of this line. Keeping in mind that the line formation process for this line has a low efficiency ($\sim$0.3%, as derived by Martin et al. 2006, and the present paper), then the He II λ4686 line reveals a powerful transient energy source in the central region of the system, a peculiar state which encouraged us to study this spectral line in greater temporal detail.

The He II λ4686 line has been studied in other colliding wind binaries such as HD5980 (Koenigsberger et al. 2010; Breysacher & François 2000; Moffat et al. 1998), V444 Cygni (Marchenko et al. 1997; Flores et al. 2001), WR127 (de la Chevrotière et al. 2011), and R145 (Schnurr et al. 2009). In those systems, it is not easy to isolate the contribution from the WWC, since the stellar winds themselves make an important contribution to the emission (e.g., in the case of V444 Cygni, the WWC region contributes only $\sim$10% of the He II λ4686 emission; Marchenko et al. 1997; Flores et al. 2001). Since the line emission is

---

[22] In this paper, phase ϕ is given by $\phi = (\mathrm{JD} - \mathrm{JD}_0)/2022.7$, where $\mathrm{JD}_0 = 2{,}452{,}819.2$ is the time when the narrow component of He I λ6678 reached its minimum value during event 11.
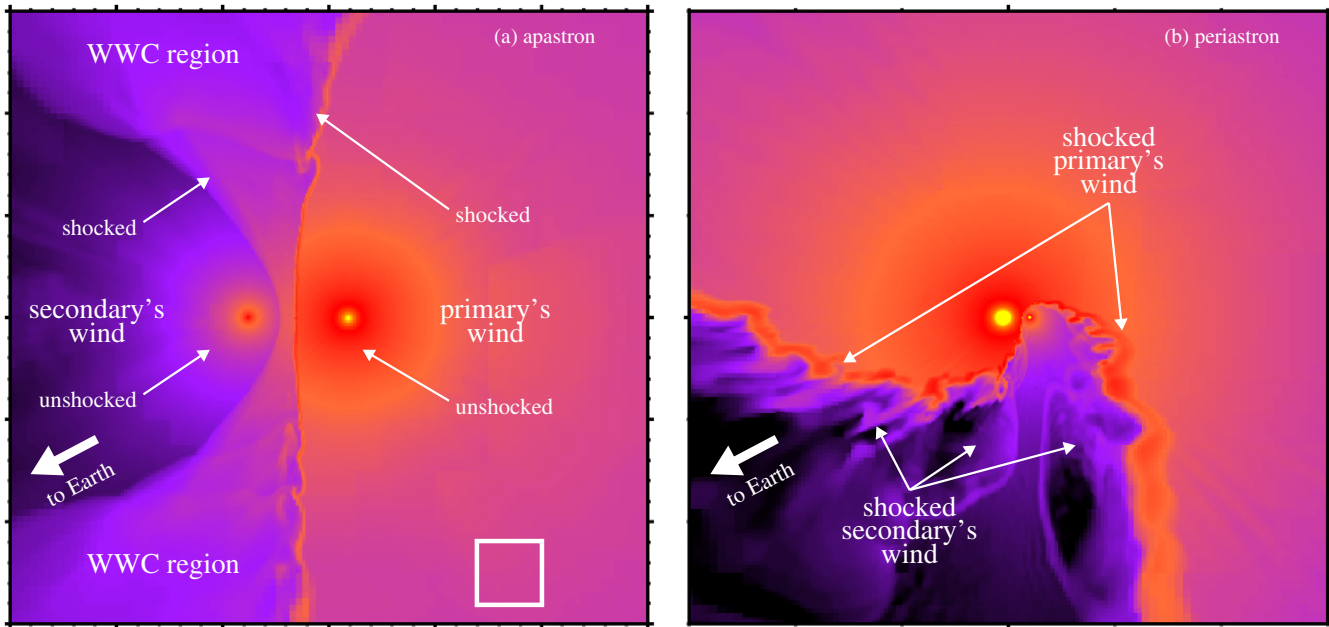
Figure 1. Snapshots of 3D simulations from Parkin et al. (2011): (a) the inner $\pm 15 \times 10^{14}$ cm of the system at apastron and (b) the inner $\pm 3 \times 10^{14}$ cm of the system at periastron. For comparison, the small box at the bottom of panel (a) has the same dimensions as the entire figure in panel (b). In both panels, the thick arrow indicates the observer's line of sight corresponding to a longitude of periastron $\omega = 243°$ (the observer is located to the lower left).
(A color version of this figure is available in the online journal.)

very faint far from periastron in η Car, the emission around periastron can be associated entirely with the WWC. There are other examples of spectral lines being formed exclusively in the WWC in other WC+O binaries, like the C III $\lambda 5696$ excess in WR140 (Fahed et al. 2011), Br22 (Bartzakos et al. 2001), and θ Mus (Hill et al. 2002).

There are only two plausible regions in the system that could produce the observed He II $\lambda 4686$ emission near periastron in η Car: the shocked stellar wind of the primary or that of the secondary star. The latter seems insufficient to produce enough He^{++} ions for recombination due to its high temperature and low density (Martin et al. 2006), whereas the former seems to have the most favorable physical conditions (e.g., density, temperature, and velocity field) for that process to occur.

Martin et al. (2006) showed that UV photons with $h\nu >$ 13.6 eV could ionize He$^+$ excited to the $n = 2$ level to He^{++} and that hydrogen-Lyα could also excite He$^+$ ions from the $n = 2$ to $n = 4$ level, which would produce the He II $\lambda 4686$ line via electronic cascade. This could happen along the WWC region, where the gas has a relatively low temperature ($T < 10^5$ K). Therefore, the He II $\lambda 4686$ emission would be somewhat connected to the hard X-ray source, but not spatially coincident with it, and the temporal behavior of both emissions should be similar. Also, the secondary star evacuates a cavity in the primary's wind near periastron, which could provide an additional source of UV photons from the inner wind of the primary. However, this emission would probably deliver much less energy than is required to power the He II $\lambda 4686$ line: $|EW| \sim 0.1$ Å (Martin et al. 2006).

The main goal of our observing campaign is to constrain the physical emission mechanism and to determine the particular location of the He II $\lambda 4686$ emitting region. The present paper is organized as follows. In Section 2, the observations and data processing are presented. In Section 3, the adopted methodology for measuring the equivalent width and velocities of the He II $\lambda 4686$ line are shown. In Section 4, we present the results

and in Section 5 the discussion. Finally, our main conclusions are shown in Section 6.

2. OBSERVATIONS AND DATA REDUCTION

We used the terminology of Groh & Damineli (2004) in naming the cycles: 1 starts in 1948 (the first low-excitation event recorded by Gaviola 1953) and the last one in 2009, which is cycle 12. In this paper, we use the term "low-excitation event" (or just "event") to refer to the disappearance of high-excitation spectral lines, which are used to define the spectroscopic cycle. We also used the term "spectroscopic cycle" to refer to the time interval between two consecutive low-excitation events (5.538 yr; Damineli et al. 2008a). The time of periastron passage is not known so we assign $\phi = 0$ to the minimum of the narrow component of the He I $\lambda 6678$ emission line, which occurred on JD $= 2,452,819,2$ for event 11 (Damineli et al. 2008b). We follow those authors also for the period length ($P = 2022.7 \pm 1.3$ days), determined by minimization of residuals when folding light curves around the minimum in cycles 9, 10, and 11. This period is very robust, since it is based on the best-sampled light curves, including the X-ray, optical, and near-infrared broadband light curves, and from variations in the strengths of several spectral lines.

2.1. Event 12 (2009.0 Minimum)

The 2009.0 minimum was spectroscopically monitored using five astrophysical observatories: Southern Astrophysical Research Telescope (SOAR/Chile), Observatório Pico dos Dias (OPD/Brazil), European Southern Observatory (ESO/Chile), Complejo Astronómico El Leoncito (CASLEO/Argentina), and Las Campanas Observatory (LCO/Chile). All the relevant data about the results presented in this paper are listed in Table 1.

Daily monitoring of the optical spectrum of η Car was carried out at SOAR from 2008 December 21 through 2009 January 23. After that, data were obtained once per month.

Table 1
Journal of Observations and Measurements for the Low-excitation Events 9, 10, 11, and 12

JD	Cycle + Phase	Equivalent Width (Å)	Radial Velocity of the Peak[a] (km s^{-1})	Observatory + Instrument
2448776.4	9.001	-1.27 ± 0.10	-293	OPD+Coudé
2448794.5	9.010	-0.31 ± 0.10	-75	ESO/La Silla+FLASH/HEROS
2448825.5	9.025	-0.56 ± 0.10	-25	ESO/La Silla+FLASH/HEROS
2448830.5	9.028	-0.36 ± 0.10	-10	ESO/La Silla+FLASH/HEROS
2448839.5	9.032	-0.26 ± 0.10	-40	ESO/La Silla+FLASH/HEROS
2448844.5	9.035	-0.19 ± 0.10	-35	ESO/La Silla+FLASH/HEROS
2450771.1	9.987	-1.93 ± 0.10	-240	MSSSO+Coudé
2450808.2	10.006	0.20 ± 0.10	N.M.	MSSSO+Coudé
2450869.9	10.036	-0.19 ± 0.10	-34	MSSSO+Coudé
2450896.1	10.049	-0.15 ± 0.10	-10	MSSSO+Coudé
2452773.5	10.977	-0.72 ± 0.12	-45	OPD+Coudé
2452803.5	10.992	-1.48 ± 0.10	-248	OPD+Coudé
2452811.4	10.996	-2.21 ± 0.55	-266	OPD+Coudé
2452812.4	10.996	-2.67 ± 0.10	-264	OPD+Coudé
2452813.5	10.997	-2.30 ± 0.12	-295	OPD+Coudé
2452814.4	10.997	-2.36 ± 0.63	-349	OPD+Coudé
2452815.4	10.998	-2.80 ± 0.14	-356	OPD+Coudé
2452816.4	10.998	-2.88 ± 0.13	-356	OPD+Coudé
2452817.4	10.999	-2.48 ± 0.10	-368	OPD+Coudé
2452818.4	10.999	-1.93 ± 0.10	-390	OPD+Coudé
2452819.4	11.000	-1.75 ± 0.14	-405	OPD+Coudé
2452820.5	11.000	-1.16 ± 0.10	-432	OPD+Coudé
2452821.4	11.001	-0.48 ± 0.39	-442	OPD+Coudé
2452822.4	11.001	-0.29 ± 0.11	-402	OPD+Coudé
2452823.4	11.002	-0.09 ± 0.11	-460	OPD+Coudé
2452825.5	11.003	0.00 ± 0.10	N.M.	OPD+Coudé
2452826.4	11.003	-0.08 ± 0.10	N.M.	OPD+Coudé
2452827.4	11.004	-0.08 ± 0.10	N.M.	OPD+Coudé
2452828.4	11.004	-0.07 ± 0.10	N.M.	OPD+Coudé
2452830.5	11.005	-0.09 ± 0.10	N.M.	OPD+Coudé
2452841.4	11.011	-0.65 ± 0.16	-24	OPD+Coudé
2452987.7	11.083	-0.12 ± 0.17	-1	OPD+Coudé
2454190.7	11.678	-0.04 ± 0.12	-97	OPD+Coudé
2454311.4	11.737	-0.07 ± 0.13	-1	OPD+Coudé
2454595.4	11.878	-0.07 ± 0.12	$+5$	OPD+Coudé
2454596.5	11.878	-0.11 ± 0.10	$+4$	OPD+Coudé
2454598.4	11.879	-0.08 ± 0.10	-4	OPD+Coudé
2454774.5	11.966	-0.55 ± 0.20	-50	LCO+MIKE
2454774.8	11.967	-0.55 ± 0.20	-50	LCO+MIKE
2454784.9	11.972	-0.43 ± 0.20	-75	LCO+MIKE
2454786.0	11.972	-0.42 ± 0.05	-70	CASLEO+EBASIM
2454787.0	11.973	-0.34 ± 0.01	-75	CASLEO+EBASIM
2454803.8	11.981	-0.61 ± 0.16	-101	SOAR+Goodman
2454809.8	11.984	-1.32 ± 0.14	-109	SOAR+Goodman
2454815.8	11.987	-2.19 ± 0.20	-127	LCO+MIKE
2454815.8	11.987	-2.30 ± 0.11	-154	SOAR+Goodman
2454821.7	11.990	-1.71 ± 0.12	-175	SOAR+Goodman
2454821.8	11.990	-1.74 ± 0.11	-155	ESO/La Silla+FEROS
2454822.9	11.990	-1.81 ± 0.10	-153	ESO/La Silla+FEROS
2454823.8	11.991	-1.78 ± 0.11	-151	ESO/La Silla+FEROS
2454824.8	11.991	-1.69 ± 0.11	-163	ESO/La Silla+FEROS
2454825.8	11.992	-1.75 ± 0.11	-156	ESO/La Silla+FEROS
2454826.8	11.992	-1.65 ± 0.11	-146	SOAR+Goodman
2454827.8	11.993	-1.70 ± 0.14	-195	SOAR+Goodman
2454827.9	11.993	-1.61 ± 0.11	-163	ESO/La Silla+FEROS
2454828.8	11.993	-1.53 ± 0.10	-166	SOAR+Goodman
2454828.9	11.993	-1.49 ± 0.12	-168	ESO/La Silla+FEROS
2454829.8	11.994	-1.45 ± 0.11	-187	SOAR+Goodman
2454829.9	11.994	-1.40 ± 0.11	-196	ESO/La Silla+FEROS
2454830.8	11.994	-1.47 ± 0.10	-260	SOAR+Goodman
2454830.9	11.994	-1.46 ± 0.10	-228	ESO/La Silla+FEROS
2454831.8	11.995	-1.87 ± 0.11	-255	SOAR+Goodman
2454831.9	11.995	-1.85 ± 0.12	-250	ESO/La Silla+FEROS

Table 1
(Continued)

JD	Cycle + Phase	Equivalent Width (Å)	Radial Velocity of the Peak[a] (km s^{-1})	Observatory + Instrument
2454832.9	11.995	-2.55 ± 0.11	-224	ESO/La Silla+FEROS
2454833.9	11.996	-2.77 ± 0.11	-218	ESO/La Silla+FEROS
2454834.8	11.996	-2.48 ± 0.11	-269	SOAR+Goodman
2454834.9	11.996	-2.54 ± 0.11	-248	ESO/La Silla+FEROS
2454835.0	11.996	-2.34 ± 0.01	-314	CASLEO+REOSC
2454835.8	11.997	-2.40 ± 0.10	-319	SOAR+Goodman
2454836.0	11.997	-2.49 ± 0.01	-378	CASLEO+REOSC
2454837.0	11.997	-2.40 ± 0.01	-362	CASLEO+REOSC
2454837.8	11.998	-2.57 ± 0.13	-341	SOAR+Goodman
2454838.0	11.998	-2.08 ± 0.01	-336	CASLEO+REOSC
2454839.8	11.999	-1.90 ± 0.13	-340	SOAR+Goodman
2454840.0	11.999	-1.91 ± 0.01	-349	CASLEO+REOSC
2454841.0	11.999	-1.79 ± 0.01	-370	CASLEO+REOSC
2454841.8	12.000	-1.67 ± 0.12	-362	SOAR+Goodman
2454842.0	12.000	-1.87 ± 0.01	-383	CASLEO+REOSC
2454842.8	12.000	-1.48 ± 0.10	-389	SOAR+Goodman
2454843.7	12.001	-1.21 ± 0.12	-412	OPD+Coudé
2454843.8	12.001	-0.93 ± 0.10	-420	SOAR+Goodman
2454844.0	12.001	-0.65 ± 0.01	-427	CASLEO+REOSC
2454844.7	12.001	-0.89 ± 0.11	-387	OPD+Coudé
2454844.8	12.001	-0.63 ± 0.11	-424	SOAR+Goodman
2454845.0	12.001	-0.63 ± 0.01	-452	CASLEO+REOSC
2454845.8	12.002	-0.32 ± 0.10	-393	SOAR+Goodman
2454846.8	12.002	-0.09 ± 0.11	-411	SOAR+Goodman
2454847.0	12.002	-0.04 ± 0.01	-425	CASLEO+REOSC
2454847.8	12.003	0.04 ± 0.10	N.M.	SOAR+Goodman
2454848.0	12.003	0.02 ± 0.01	N.M.	CASLEO+REOSC
2454848.8	12.003	-0.00 ± 0.20	N.M.	LCO+MIKE
2454849.0	12.003	-0.09 ± 0.01	N.M.	CASLEO+REOSC
2454850.0	12.004	0.08 ± 0.01	N.M.	CASLEO+REOSC
2454852.0	12.005	-0.05 ± 0.01	N.M.	CASLEO+REOSC
2454853.0	12.005	-0.02 ± 0.01	N.M.	CASLEO+REOSC
2454853.7	12.006	-0.13 ± 0.11	N.M.	SOAR+Goodman
2454854.0	12.006	-0.12 ± 0.11	N.M.	CASLEO+REOSC
2454854.8	12.006	$+0.01 \pm 0.20$	N.M.	LCO+MIKE
2454855.0	12.006	-0.07 ± 0.11	N.M.	CASLEO+REOSC
2454859.8	12.009	-0.42 ± 0.11	-90	SOAR+Goodman
2454871.5	12.014	-0.76 ± 0.20	-50	LCO+MIKE
2454871.7	12.014	-0.70 ± 0.11	-209	SOAR+Goodman
2454882.6	12.020	-1.18 ± 0.12	-15	OPD+Coudé
2454883.7	12.021	-1.13 ± 0.20	0.	LCO+MIKE
2454888.5	12.023	-1.03 ± 0.12	$+6$	SOAR+Goodman
2454898.0	12.027	-0.11 ± 0.08	0	CASLEO+EBASIM
2454899.5	12.028	-0.24 ± 0.11	$+3$	SOAR+Goodman
2454905.0	12.031	-0.40 ± 0.33	0	CASLEO+REOSC
2454906.0	12.031	-0.20 ± 0.07	0	CASLEO+REOSC
2454907.0	12.032	-0.18 ± 0.32	0	CASLEO+REOSC
2454925.5	12.041	-0.10 ± 0.11	$+7$	SOAR+Goodman
2454940.5	12.048	-0.32 ± 0.11	$+0$	OPD+Coudé
2454942.5	12.049	-0.07 ± 0.11	-9	SOAR+Goodman
2454953.5	12.055	-0.06 ± 0.11	-21	SOAR+Goodman
2454953.6	12.055	-0.00 ± 0.11	$+13$	ESO/La Silla+FEROS
2454955.6	12.056	-0.01 ± 0.11	$+13$	ESO/La Silla+FEROS
2454967.5	12.062	0.02 ± 0.11	$+14$	SOAR+Goodman
2455368.4	12.260	-0.05 ± 0.14	-100	OPD+Coudé
2455754.8	12.451	-0.10 ± 0.10	$+30$	OPD+Coudé

Note. [a] Velocity of the highest point of the fitting of the He II λ4686 line profile. In this table, the flag N.M. (*not measurable*) indicates when the line is absent (or very weak) and when the peak velocity is impossible to measure.

The Goodman optical spectrograph was used to obtain spectra with spectral resolving power $R \sim 2800$ (3 pixels) in the range $\lambda\lambda 3500$–6850. All the observations were performed using the 0.45 arcsec wide slit aligned with the parallactic angle. For each visit, a hot standard star (HD 303308; O4.5 v((fc)); Walborn et al. 2010; Sota et al. 2011) was observed to correct for telluric lines and for low-frequency variations in the detector response along the spectral dimension. Processing, reduction, and calibration of the SOAR data were done using the standard long-slit spectroscopic packages of IRAF[23] (Tody 1993). The one-dimensional spectrum was extracted using the IRAF package DOSLIT and the spatial extraction aperture was about 1.5 arcsec for all the SOAR spectra. Performing extractions with apertures as large as 4.5 arcsec does not introduce any significant change in either the He II $\lambda 4686$ line profile or in the measured equivalent widths. Before or after each set of observations of η Car, two exposures of an HgAr/CuAr lamp were obtained for wavelength calibration.

The fiber-fed extended-range échelle spectrograph (FEROS) data were obtained at the 2.2 m telescope (Max Planck Institute). FEROS delivers data with resolving power $R \sim 48,000$ (2 pixels) and spectral coverage from 3700 to 8600 Å in a single exposure. It uses two fibers with diameter of 2 arcsec separated by 2.9 arcmin. The processing, reduction, and calibration were performed using the FEROS standard reduction pipeline, which is described in Kaufer et al. (1999).

Spectra were also measured at the Coudé focus of the 1.60 m telescope of the Pico dos Dias Observatory (OPD/Brazil), with $R \sim 10,000$ (2 pixels). For each visit, a hot star (θ Car; B0.2 v; Hubrig et al. 2008; Nazé & Rauw 2008) was also observed to correct the shape of the continuum for the variations in the instrument's response. The size of the extraction aperture for the OPD data was about 2 arcsec. A ThAr spectrum was obtained immediately preceding or following the η Car observations for wavelength calibration.

We also obtained spectra at the 6.5 m Magellan telescope located at Las Campanas Observatory, using the échelle spectrograph MIKE, with $R \sim 25,000$ (2 pixels) in the blue region. MIKE's data processing was performed by cutting from the raw échelle images only the orders that contained the He II $\lambda 4686$ line and its continuum region (orders from 75 to 78). Using this approach, we could process, reduce, and calibrate the data using typical IRAF échelle routines. For those data, we used the spectrum of a hot standard star (HD 303308, the same one used for the SOAR data set) for a first rectification of the low-frequency variations along the spectral dimension.

Spectroscopic data were also obtained with the EBASIM and REOSC spectrographs at the CASLEO Observatory 2.15 m telescope. Both are échelle spectrographs with $R \sim 42,000$ and $R \sim 12,000$, respectively. The data reduction and processing were performed using standard IRAF tasks for échelle data.

The signal-to-noise ratio (S/N) of the data from the 2009.0 campaign was always higher than 100 for all these observations, frequently reaching S/N ~ 250.

2.2. Previous Events: 9 (1992.5), 10 (1998.0), and 11 (2003.5)

The data from previous events shown in the present paper were obtained at the Coudé focus of OPD and with the FLASH/HEROS spectrograph at the ESO 0.52 m telescope

(events 9 and 11; we would like to remark that the ESO data set for event 9, used in the present work, was wrongly assigned to OPD in Steiner & Damineli 2004). Spectra were also taken on 1997 November and December, and 1998 February and March, at the Coudé focus of the 1.9 m telescope of the Mount Stromlo and Siding Spring Observatory (MSSSO) with $R \sim 60,000$ in the range from 4346 to 4935 Å (McGregor et al. 1999).

3. MEASUREMENT METHODOLOGY FOR THE He II $\lambda 4686$ LINE

In order to have a homogeneous data set and to minimize systematic errors, we first identified the region to be considered as the He II $\lambda 4686$ reference continuum. Figure 2 illustrates the regions we adopted for the integration and continuum, which were set to a small wavelength interval (3 Å wide) near 4610 Å and 4740 Å. Since the spectra were previously flattened using the spectrum of a hot star, the continuum in this range is well represented by a linear fit, and the equivalent width was measured by direct integration of the line profile in the range from 4675 to 4694 Å. The regions defined in this work for the line integration and continuum are very similar to those adopted by Martin et al. (2006) using *Hubble Space Telescope* data.

In order to have a robust determination of the radial velocity of the line peak, we used a two-Gaussian model to fit the integration region of the line profile, since a single-Gaussian profile did not reproduce the line profile over the integration region across the low-excitation event, especially when the equivalent width reaches its maximum value near $\phi = 0$. Figure 2 shows the two-Gaussian components used to fit the He II $\lambda 4686$ line profile. The resulting two-component fit was then used to find the wavelength at which the line profile reaches its peak intensity. Note that, since we are interested only in the radial velocity of the line peak, the line wings, which are much more extended, do not influence the derived velocity of the line peak. All of the radial velocities measured in the present paper are in the heliocentric frame.

The main source of uncertainties in the methodology for measuring the equivalent width is the normalization of the continuum. Data obtained in échelle mode suffer from order overlap and corrections for this overlap are crucial for tracking the real stellar continuum. We normalized the échelle spectra in two steps. First, we divided the flat-fielded spectrum by the continuum of a hot star, then we applied a parabolic fit to finally rectify the continuum. We rejected data in which the rectified continuum showed low-frequency variations greater than 1%.

As mentioned previously, the wavelength calibration was obtained using comparison lamps. It is impossible to ascribe a single representative error to the entire observational data set because each instrument has its own characteristics, reduction procedure, and calibration methods. However, we checked the reliability of our procedure by comparing multiple observations taken on different telescopes in the same night. Discrepancies in velocity are smaller than 50 km s^{-1}. Equivalent width measures from different telescopes at similar phases are also in quite good agreement.

We claim that our set of He II $\lambda 4686$ spectra is the most accurate reported so far. It has the best time sampling over the last two events (11 = 2003.5 and 12 = 2009.0) in addition to some data for cycles 9 and 10. Also, ground-based spectra—because they are spatially unresolved—are very robust for time variation studies, since most of the emission comes from ~ 1 arcsec around the central source, which is blurred by the seeing so that
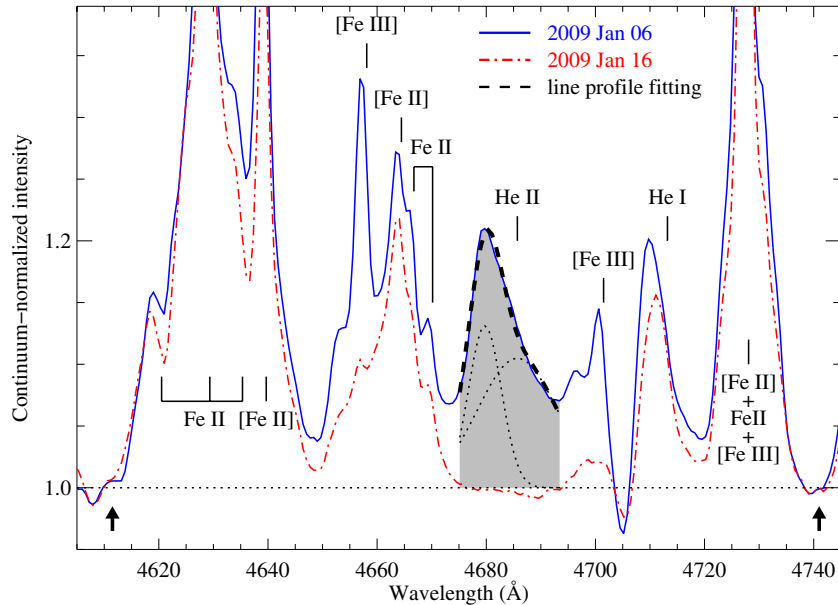

Figure 2. He II λ4686 at minimum (dash-dotted red line) and maximum (solid blue line). The observed line profile was fitted by two-Gaussian components (dotted lines) and the result (dashed line) was used to measure the radial velocity. The two arrows indicate the regions adopted as continuum level for the He II λ4686 emission line. The equivalent width was derived by direct integration under the line profile (gray shaded area).

(A color version of this figure is available in the online journal.)

the ground-based slit is always sampling the relevant emitting region.

The absence of He II λ4686 emission on MJD 52852 reported by Martin et al. (2006) might be caused by a bad datum or a real momentary fading of the line. Despite the fact that we cannot directly compare the results because we do not have simultaneous ground-based data, we call attention to the fact that our monitoring along 3 cycle (9, 11, and 12) always show this line in emission, confirming that P3 is a repeatable feature. Anyway, this point can be clarified in the next event (in 2014.6).

4. RESULTS

The observed He II λ4686 equivalent width curve is shown in Figure 3, which presents data for the last four events (9, 10, 11, and 12) using the following ephemerides:

$$\mathrm{JD} = \mathrm{JD}_0 + 2022.7(E - 11), \qquad (1)$$

where $\mathrm{JD}_0 = 2,452,819.2$ (time of minimum intensity of He I λ6678; Dameneli et al. 2008b) and E is the cycle+phase count. We focused on a time interval ranging from 2 months before up to 4 months after $\phi = 0$. In this paper, we use the word "day" as a reference to the number of days before (indicated by a minus sign) or after (plus sign) $\phi = 0$ for each cycle.

The 2003.5 spectra used to measure the equivalent width and radial velocities shown in this paper are the same as those presented in Steiner & Dameneli (2004) but reduced according to the procedures described in Section 2 in order to keep the whole set of data as homogeneous as possible. Figure 4 shows that He II λ4686 was detected with EW ~ -0.1 Å in a spectrum taken at the OPD telescope on 2008 May 8, about 8 months before the low-excitation event, and also at the same strength in another spectrum taken 17 months after $\phi = 0$, on 2010 June 20 (using the same telescope and instrumental configuration). Another spectrum, taken on 2011 July 11, at $\phi = 12.451$—almost apastron—also shows a very faint emission, which may be

He II λ4686. These observations[24] suggest that He II λ4686 is present, except for a 5 day interval after the start of the spectroscopic event, along the whole 5.538 yr cycle (Steiner & Dameneli 2004), though Martin et al. (2006) claimed that this line is not present at any phase outside the low-excitation event. The observed continuum-normalized time series spectrum of η Car in the region λλ4660–4710 is shown in Figure 5. In that figure, we interpolated the spectra in phase to show the temporal evolution of the He II λ4686 emission line. Notice that Figure 5 mainly reflects the progression of the cycle 11 to 12 since data are sparse for other cycles.

A major feature in the intensity curve for event 12 is the presence of three local maxima (labeled in Figures 3 and 5 as P1, P2, and P3). The first local maximum, P1, occurred about day −26, and showed a conspicuous peak with EW = −2.30 Å. The second local maximum, P2, occurred between day −10 and −5, and during this time interval, the mean equivalent width was about −2.5 Å. After day −5, the equivalent width of the line rapidly decreased to zero and it completely disappeared by day +5. From day +5 to +10 the equivalent width was zero. After day +10 it started to increase again, to a local maximum value of −1.2 Å (P3) at day +40, and then decreased to −0.1 Å after day +115. The rate of decrease of the EW just before minimum was about −0.3 Å per day and the *e*-folding timescale in the fading phase (after P2) was ∼2 days.

There are only a few sparse data near the low-excitation event for cycles earlier than cycle 12 (except for cycle 11 in 2003.5, as shown in Steiner & Dameneli 2004); despite this we can see that the general behavior of the equivalent width of the He II λ4686 line repeats faithfully from cycle to cycle. Peaks P1 and P2, however, do not seem to be phase-locked: for event 12, P2 (the best time sampled peak) occurred ∼4 days before the phase in which it was detected in event 11 (see inset in Figure 3). Although there were no data in the earlier cycles corresponding

---

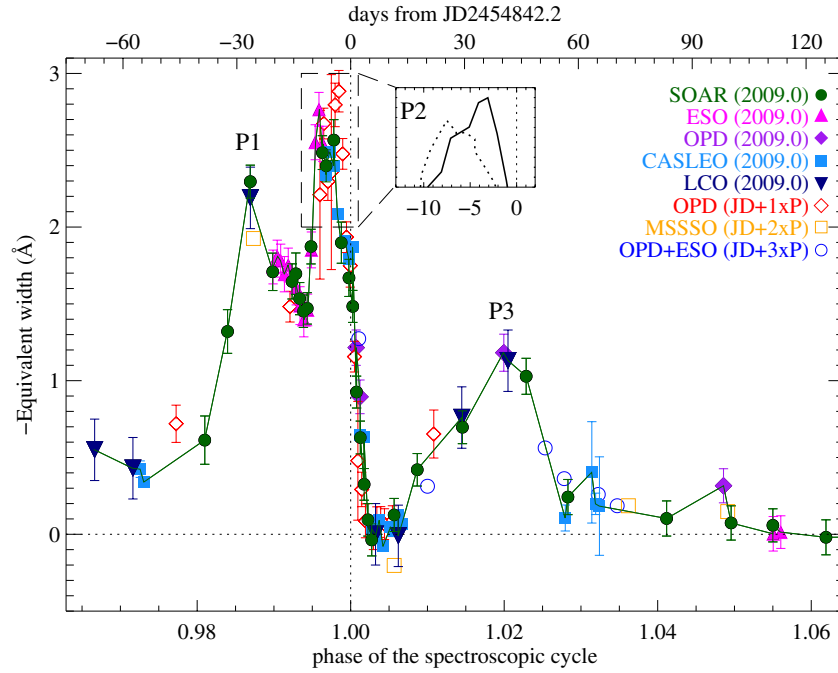[24] Notice that none of them are included in Figure 3 because they are far from the low-excitation event.

Figure 3. Equivalent width of He II λ4686 for the 2009.0 event (filled symbols) and for past events (open symbols) taken at different observatories. Data from the three previous events are overplotted as empty symbols, and folded with a period of $P = 2022.7$ days. Each local peak discussed in the text is labeled in this figure as P1, P2, and P3. The inset panel shows the mean value of the equivalent width around peak P2 for event nos. 11 (solid line) and 12 (dotted line) and illustrates that the peaks do not seem to be phase-locked. Indeed, for event no. 12, P2 occurred ~4 days before the phase observed for event no. 11.

(A color version of this figure is available in the online journal.)

to the phase of the peak P3 maximum, the behavior of the line equivalent widths observed in the 1992.5 and 2003.5 events (see Figure 3) suggests that P3 is a phase-locked feature.

4.1. He II λ4686 Luminosity

The intrinsic line luminosity L^0 of He II λ4686 is given by

$$L^0 = 4\pi D^2 f^0_{\lambda 4686} \, \mathrm{EW}_{\mathrm{He\,II\,\lambda4686}}, \qquad (2)$$

where D is the distance to the system (2.3 kpc), $\mathrm{EW}_{\mathrm{He\,II\,\lambda4686}}$ is the equivalent width of the He II λ4686 line (measured in the present work), and $f^0_{\lambda 4686}$ is the intrinsic flux from the central source near $\lambda = 4686$ Å. We assume that $f^0_{\lambda 4686} \approx f^0_B$, where f^0_B is the dereddened B-band flux from the source. The observed B-band flux (f^{obs}_B) is derived from observed B-band magnitudes following this relation:

$$f^{\mathrm{obs}}_B = 6.5 \times 10^{-10} \times 10^{-0.4B}, \qquad (3)$$

where B is the observed B-band brightness of the central source, as obtained by Fernandez Lajus et al. (2009). It is important to remark that Fernandez Lajus et al. (2009) used a 12″ radius aperture, which includes the entire Homunculus—an important source of scattered light. In order to match the 1″ region sampled by the ground-based spectroscopy, we used a B-band image to determine the magnitude difference between a 1″ circular aperture centered on the star and the 12″ aperture used for the rest of the photometry. This showed that the B-band magnitudes reported by Fernandez Lajus et al. (2009) needed to be fainter by +1.6 mag to match the spectral aperture. The dereddened flux at 4686 Å is then given by

$$f^0_{\lambda 4686} \approx f^0_B = f^{\mathrm{obs}}_B \times 10^{0.4 A_B}, \qquad (4)$$

where A_B is the extinction in the B band. However, since we have no direct measurement of A_B, we adopt the usual value for A_V (Davidson et al. 1995; Hillier et al. 2001) to obtain A_B using the following linear relation from Cardelli et al. (1989):

$$\frac{A_B}{A_V} = a(\lambda) + \frac{b(\lambda)}{R_V}, \qquad (5)$$

where $a(\lambda)$ and $b(\lambda)$ are constants which depend on the wavelength and, in the present work, need to be evaluated in the B-band region ($\lambda = 4500$ Å).

The secular brightening of η Car has been interpreted as a decrease in extinction (see van Genderen et al. 2006), probably due to an expansion in the circumstellar shell, so we need to estimate the decrease of A_V with time. In 1998, in the line of sight to the central source there were about $A_V = 7$ mag of total extinction (interstellar and circumstellar; Hillier et al. 2001) from which ~2 mag were due to gray extinction associated with large grains around the central source. Based on this result, in early 2006 the estimated extinction was $A_V = 5.7$ (van Genderen et al. 2006). From 2003 to 2009, the average rate of increase in the brightness of the central source was -0.06 mag yr^{-1}. Therefore, the total extinction to the central source in 2003.5 was $A_V = 5.9$, and in 2009.0, $A_V = 5.5$. We do not correct for the scattering in the primary's wind, which should contribute to a cyclic variability in A_V.

In order to transform from A_V to A_B, we used Equation (5), with $R_V = 4.9$ (Hillier et al. 2001; van Genderen et al. 2006). Hence, with the photometry in the B band and the total extinction A_B, we were able to calculate the intrinsic flux $f^0_{\lambda 4686}$ and thus the intrinsic luminosity of the He II λ4686 emission line from Equation (2).

The results are shown in Figure 6(a), where the intrinsic line luminosities are shown—as well as the photon fluxes—for two events: 2003.5 and 2009.0. The line luminosity of the 2003.5
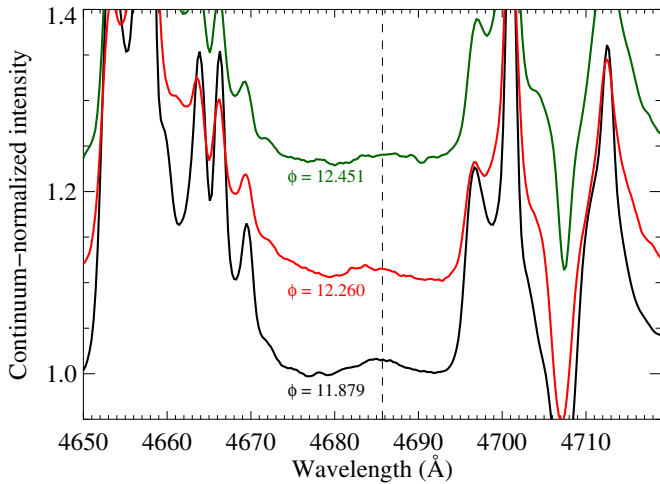
Figure 4. Spectra of η Car taken on 2008 May 10 ($\phi = 11.879$; black line), 2010 June 20 ($\phi = 12.260$; red line), and 2011 July 11 ($\phi = 12.451$; green line), showing the presence of He II $\lambda4686$ at 8 months before, 17 months after, and 31 months after the event, respectively (spectra taken at the OPD/Coudé). The corresponding phase of the spectroscopic cycle is also indicated. He II $\lambda4686$ far from periastron is present at faint level, EW< -0.1 Å.

(A color version of this figure is available in the online journal.)

event was higher than that of 2009.0 (for a given phase): the peak values for the intrinsic line luminosity were, respectively, 310 $L_\odot$ (corresponding to 1.8×10^{47} He II $\lambda4686$ photons per second) and 250 $L_\odot$ (=1.4×10^{47} He II $\lambda4686$ photons per second). We cannot claim that there is a real difference in the intrinsic luminosity, since the extinction might have varied in shorter timescales than we adopted. These luminosities are probably lower limits to the true line luminosity since the adopted correction for extinction is only a simple estimate, and because obscuration by the wind of the primary star could also be significant.

4.2. Radial Velocities

During most of the spectroscopic cycle, the radial velocity of the line peak was close to zero. Near the low-excitation event, there were two regimes for the rate of change in the radial velocity (shaded areas R1 and R2 in Figure 6(b)). Region R1 is near day -90 when the radial velocity of the line peak changed at a daily rate of about -2 km s^{-1} (shifting from -50 km s^{-1} on day -67 to about -150 km s^{-1} on day -17). The first peak in the equivalent width (P1) occurred during this time interval, on day -26. The second regime (R2) started on day -17 and was observed until the line completely disappeared, on day $+6$. During this time interval, the rate of change in the radial velocity of the line peak was almost seven times greater than in the previous interval: it started at -150 km s^{-1} on day -17, and reached -450 km s^{-1} on day $+5$, a change of nearly 14 km s^{-1} per day. Between day $+6$ and $+15$ the line could not be measured.

The general behavior of the He II $\lambda4686$ radial velocity suggests that this line is formed in the WWC region, in the interval from 2 months before to 2 months after the minimum. This is supported by the observed velocity of the X-ray line S XVI Lyα (Figure 6(b); Henley et al. 2008). The time variations in radial velocity for both lines are similar: they become more blueshifted near $\phi = 0$ and then shift to projected velocities near zero. However, the velocity of the S XVI Lyα line just prior to the low-excitation event is more than a factor of two larger than that of He II $\lambda4686$ line. This is surprising, since we expect the S XVI Lyα line to be emitted close to the apex, where the flow velocity is slower than it is downstream along the WWC region. On the other hand, near $\phi = 0$, the WWC gets very distorted and unstable, which could result in a mixed contribution from different regions.

The interpretation of the He II $\lambda4686$ radial velocity curve is not as simple as in other colliding wind systems because of the severe Coriolis distortion of the shock near periastron passage. As the stars approach periastron, the leading and the trailing
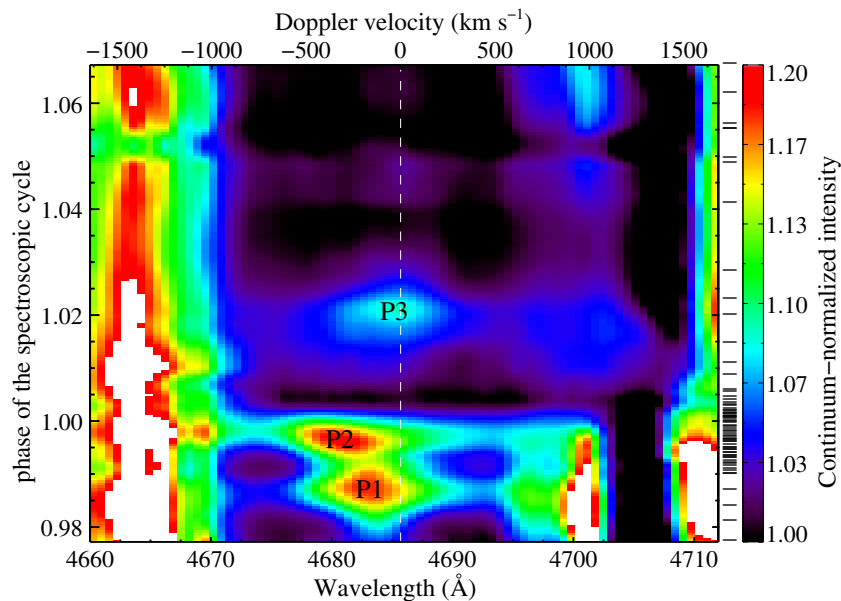

Figure 5. Folded time series spectra of the He II $\lambda4686$ line profile along the four last low-excitation events. The continuum-normalized intensity of the spectra is color-coded between 0% and 20% of the continuum level for visualization purposes. The vertical dashed line marks the rest wavelength of the He II $\lambda4686$ line emission. The tick marks located on the right, between the color bar and the image, indicate the phases when spectra were obtained.

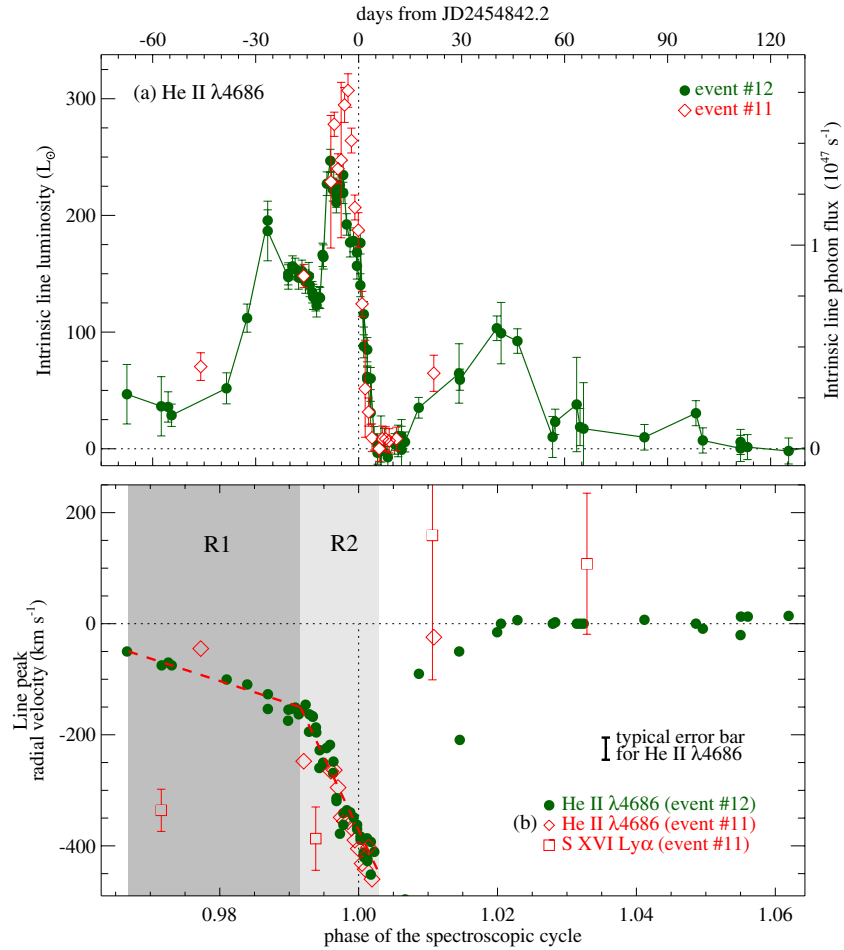(A color version of this figure is available in the online journal.)

Figure 6. (a) Lower limit for the intrinsic luminosity of the He II λ4686 line for 2009.0 (filled green circles) superimposed on the 2003.5 event (empty red diamonds) folded with a period of $P = 2022.7$ days. (b) Radial velocity of the peak of the He II λ4686 line for both events and the observed velocity of the S XVI Lyα for the 2003.5 event (red squares; data extracted from Henley et al. 2008). The shaded areas indicate the two different regimes (R1 and R2) for the rate of change in the radial velocity curve. The abscissa in panel (a) is plotted in the same timecale as in panel (b).

(A color version of this figure is available in the online journal.)

arms of the shock are subject to different drag forces and the cone is heavily distorted. In addition, the inner zones, close to the apex, revolve fast in a spiraling pattern. Because of these complications, the projected radial velocities of the gas which produces the observable emission cannot be modeled using a simpler, rigid-cone geometry as has been used effectively for other colliding wind binary systems.

It is interesting to notice that the radial velocity of the peak of the He II λ4686 line emission shifts to the blue almost at the same time as the He I λ10830 P Cyg absorption shows a high-velocity absorption component bluer than -900 km s^{-1} (Groh et al. 2010). Since the velocity field of the WWC region has a complex pattern close to periastron, we expect to see a wide range of velocities and this is in fact present in the large FWHM of those two lines. However, this interpretation may be too simple, since the absorption component samples a very limited region in our line of sight while the emission receives contributions from many other regions.

We should only see high positive velocities coming from the WWC region when it is pointing away from us, during periastron passage. Due to the high orbital eccentricity, the WWC cone does not rotate much until just before periastron passage, which means that the time spent by the WWC cone pointing away from the observer is very short. From Figure 6, it is evident that

the maximum negative radial velocity occurs for P2, which is detected between day -5 and -10. Therefore, based on symmetry arguments for the motion of the secondary around the primary, the maximum positive radial velocity should occur somewhere between day $+5$ and $+10$, which corresponds to the interval when the He II λ4686 line is absent. Note, however, that this interval coincidently may occur at the same time as the disruption of the WWC region.

The radial velocity of the peak of the He II λ4686 line profile showed the same behavior for events 11 and 12: it reached up to -450 km s^{-1} just before the minimum and completely vanished during 5 days (from day $+5$ to $+10$). After that, the peak was detected again with a radial velocity of -100 km s^{-1}, which changed to about zero ~40 days after $\phi = 0$.

4.3. Correlation between He II λ4686 and X-Rays

During the 2009.0 low-excitation event, after shifting the X-ray light curves in time by $+16.5$ days, the regime of fast decrease in the X-ray flux began approximately at the same time as the decrease in the He II λ4686 equivalent width (see Figure 7(a)). The major peaks in the X-ray flux preceding the event also seem to have counterparts in the He II λ4686 equivalent width peaks. The 2003.5 observations did not show *clearly*
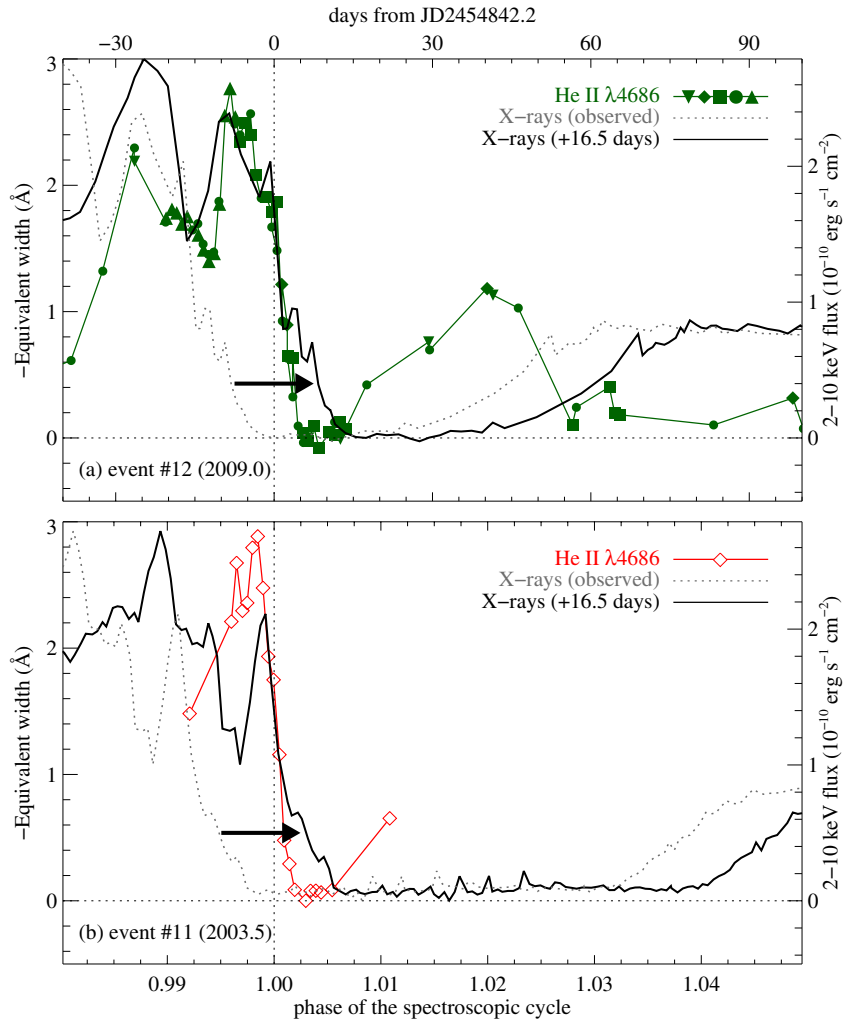
Figure 7. Equivalent width curve of He II λ4686 (symbols) overplotted with the 2–10 keV X-ray flux. In both panels, the observed X-ray flux is illustrated by the dotted gray line (from Corcoran 2005), while the solid black line was shifted by +16.5 days. Panel (a) is for cycle 12 and panel (b) is for 11.
(A color version of this figure is available in the online journal.)

the same correlation between the X-ray flares and He II λ4686 peaks (see Figure 7(b)), possibly because of sparser monitoring and/or lower quality He II λ4686 data. This suggests a possible connection between the X-ray and the He II λ4686 behavior. The delay of 16.5 days could be interpreted as the flow time of the shocked material, from the region where X-rays are created (in the WWC apex) to that where the temperature has dropped below 6×10^5 K, allowing for the recombination of He^{++} into He$^+$. If so, assuming a flow velocity of 500 km s^{-1} for the shocked material (terminal velocity of the primary's wind; Hillier et al. 2001; Pittard & Corcoran 2002), then the bulk of the He II λ4686 emission should come from a region 4–5 AU from the apex, which is consistent with the results of 3D models (Parkin et al. 2011), which predict a temperature of $\sim 10^5$ K in the primary's shocked stellar wind at that distance from the apex.

It is interesting to notice that the X-ray light curve of WR140[25] is similar to that of η Car in the sense that there is a gradual increase until a maximum, followed by a sharp decrease

(Williams 2011; Corcoran et al. 2011). The main difference between these X-ray light curves is the duration of the X-ray minimum, which is much longer for η Car (perhaps caused by the collapse of the WWC region, as discussed in the next section). Another important difference is the presence of X-rays flares in η Car when approaching periastron, which are not seen in WR140; this might suggest that in the stellar wind of the WC7 primary component of WR 140, the clumps are smaller than those in the LBV primary star in η Car (Moffat & Corcoran 2009).

4.4. He II λ4686 Far from Periastron

The faint emission seen along most of the orbit could be emitted in the WWC itself, since far from periastron, the density in the shock is smaller and the efficiency of He II λ4686 pumping is lower. However, since cooling is less efficient at lower density, the emission would occur farther from the apex, as compared to the strong emission at periastron. The speed of the shocked gas should be larger than it is near the apex, resulting in larger emission line velocities. Since at those phases the shock cone points in our direction, the observed radial velocity should be shifted to very negative values, different to what is observed, unless the opening angle of the cone increases by a large factor.

---

[25] This system is the archetypal of the colliding wind binaries and is composed of a WC7+O4-5 binary in a highly eccentric (∼0.896), long period (∼2896.5 days) orbit (see Williams et al. 1990; White & Becker 1995; Marchenko et al. 2003; Fahed et al. 2011).

In principle, the He II λ4686 emission could be formed in the inner wind of the primary star, according to models computed by Hillier et al. (2001, 2006). The problem then would be to explain its disappearance at periastron, since at that phase the primary star is at our side.

Another possibility is that the stellar wind of the secondary star would be the source of the faint He II λ4686 emission seen near apastron. Studies of the photoionization of the ejecta around the system suggest that the companion star has effective temperature between 37,000 and 43,000 K and luminosity between 10^5 and 10^6 $L_\odot$ (Mehner et al. 2010a; Verner et al. 2005; Teodoro et al. 2008). As discussed by Hillier et al. (2006), a companion star with $T_{\rm eff} = 33,000$ K and $L = 10^6$ $L_\odot$ would not have its spectral lines detected in the optical, since the flux of the primary star is at least a factor of ∼25 higher than that of the companion at those wavelengths.

In any case, if the secondary star was the source of the faint He II λ4686 line observed far from periastron, the emission should be stronger near apastron than far from it, since the WWC cavity is opened toward us at those phases (Pittard & Corcoran 2002; Okazaki et al. 2008; Parkin et al. 2009, 2011).

However, as seen in Figure 4, the emission line intensity at $\phi = 0.45$ (close to apastron) is not stronger than at $\phi = 0.26$ or at $\phi = 0.897$, when the secondary is closer to periastron. Therefore, the only region left to be responsible for the production of the He II λ4686 at apastron is the WWC shock. In the next section, we will show that this line is formed in the WWC at periastron too.

5. DISCUSSION

Peak P2 (the absolute maximum) in the intrinsic luminosity of the He II λ4686 line emission corresponds to an emitted power of 1.2×10^{36} erg s^{-1} (recall that this is a lower limit because of uncertainties in the extinction correction). This large luminosity is emitted in only a single atomic transition. The secondary wind is already excluded as the source of the emission because the mechanism of illumination of its unshocked stellar wind by the hard UV/soft X-rays produced in the WWC region, proposed by Steiner & Damineli (2004), does not account for the revised intrinsic photon flux of the He II λ4686 line. There are only two regions in which this enormous He II λ4686 luminosity could be produced: the shocked stellar wind of the primary or the shocked stellar wind of the secondary star.

Recent 3D models including inhibition effects (Parkin et al. 2009) show that the wind of the secondary star close to periastron must collide with a slower pre-shock velocity (∼1400 km s^{-1}) due to the strong radiation field of the primary star (a process known as radiative inhibition). In this case, the shocked wind of the secondary near periastron would produce emission at lower energies than if the winds collided at terminal velocity. This softer emission might lead to an increase of flux near the peak of the He$^+$ ionization threshold at 0.0544 keV.

To test this, we adopted the results of 3D simulations (Parkin et al. 2009, 2011) for the intrinsic spectral energy distribution (SED) of the shocked secondary's wind (Figure 8) and used them to calculate the total power produced in the hard UV/soft X-ray domain during periastron passage (we extrapolated the SED down to 0.0544 keV and then integrated it from 0.0544 to 0.550 keV). This model predicts an intrinsic luminosity $L^0 = 7 \times 10^{37}$ erg s^{-1} produced by the thermalization of the shocked secondary's wind. We then used the CLOUDY photoionization code to derive what fraction of the total He II recombination emission would correspond to the transition from
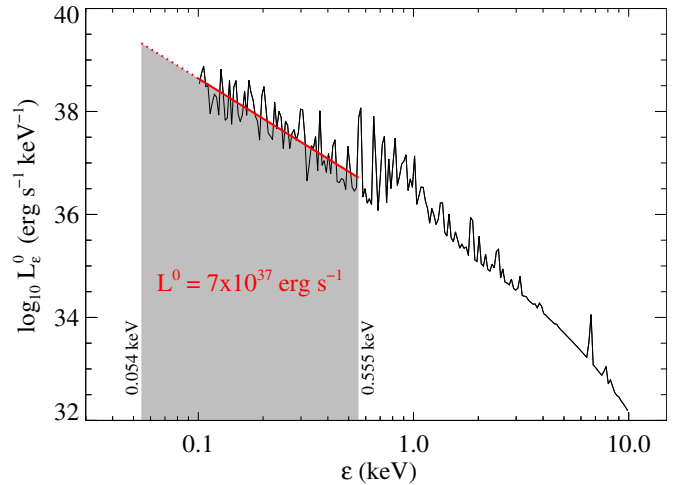

Figure 8. Calculated spectral energy distribution (SED) of the shocked secondary's wind during periastron passage (from Parkin et al. 2009). The intrinsic luminosity, L^0, was obtained by integrating the SED from 0.0544 to 0.550 keV (indicated by the gray shaded area). Notice that we fitted the SED (solid red line) and extrapolated it in the range from 0.0544 to 0.1 keV (dotted red line) because the output from simulations only goes down to 0.1 keV.

(A color version of this figure is available in the online journal.)

$n = 4$ to $n = 3$ in a high-excitation nebula with density of $n_e \sim 10^{10}$ cm^{-3} (suitable for the shocked secondary's wind). We found that He II λ4686 accounts for less than 0.3% of the total He II emission. Therefore, the secondary's thermalized shocked wind would have to have an intrinsic luminosity of

$$L^0 = \left(\frac{54.4}{4.2}\right)\left(\frac{L^{\rm obs}_{\lambda4686}}{0.003}\right) = 5.2 \times 10^{39}\ {\rm erg\ s^{-1}} \qquad (6)$$

in order to account for the intrinsic luminosity of He II λ4686. This value is almost two orders of magnitude higher than that calculated by 3D models, and therefore, we take this as strong evidence that the He II λ4686 emission line does not originate in the secondary's shocked wind (even in the most favorable case where radiative inhibition causes the shock to occur at velocities lower than terminal).

The temperature, density, and velocity of the primary's shocked stellar wind favor the production of photons with energy in the hard UV/soft X-ray domain suitable for ionizing or exciting He$^+$. Inside the high density ($n_e \sim 10^{10}$ cm^{-3}) and low temperature ($<10^5$ K) shocked primary's wind, both the photoionization due to the X-ray and stellar radiation fields increase the extent of the He^{++} region. This would naturally increase the number of recombining ions contributing to the line emission, which could account for the intrinsic luminosity of He II λ4686 near periastron. Furthermore, radiative effects in He$^+$ (Martin et al. 2006) can also increase the population in the $n = 2$ level from where He$^+$ can be easily ionized by any photon with $h\nu > 13.6$ eV (i.e., photons in the hydrogen Lyman continuum). Therefore, the intrinsic SED of the shocked primary's wind from 3D models would be of great interest to determine the exact amount of He II λ4686 emission within this region—this study, however, is beyond the scope of the present paper. Therefore, based on the intrinsically high luminosity of the He II λ4686 emission line, we exclude all other possible regions but the primary's post-shocked wind as the region where the strong emission seen near periastron is formed.

The time delay of 16.5 days between the X-ray and the He II λ4686 light curves could be determined by the time flow of
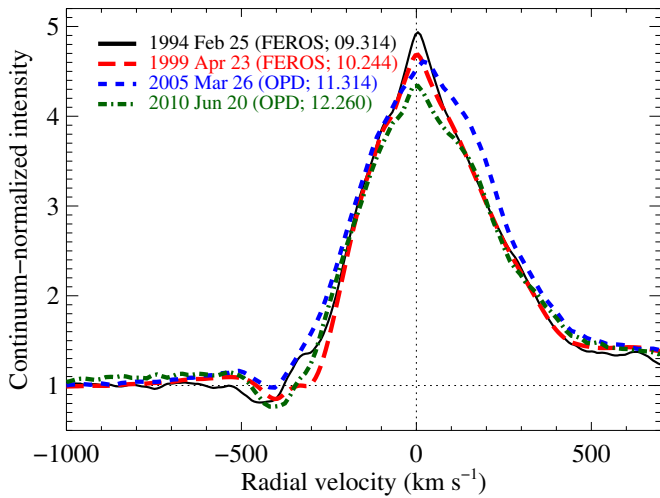
Figure 9. Continuum-normalized line profile of Hδ at approximately the same phase (indicated in the legend), along the last four cycles. Moderate variability at a low level is present, but no strong change in the line strength (which would be expected if the mass-loss rate dropped by a factor of two) was seen in any of the four cycles.

(A color version of this figure is available in the online journal.)

Figure 10. Projection of the orbital plane, relative to the position of the primary star ($e = 0.9$ and $P = 2022.7$ days). The concentric dashed circles correspond to the region of maximum emissivity of each labeled line. The gray shaded area indicates the zone where Hδ emissivity is higher than 50% of its maximum. The primary star is drawn to scale, with $R_* = 60\,R_\odot$. The red × symbols are drawn at each 0.1 in phase and the blue squares and numbers indicate the cycle+phase when the spectra shown in Figure 9 were obtained. The dashed paraboloid indicates the position of the WWC shock at $\phi = 0.8$ and stellar mass of 90 $M_\odot$ and 30 $M_\odot$ for the primary and secondary star, respectively.

(A color version of this figure is available in the online journal.)

the gas from the WWC apex up to the location where He II λ4686 is emitted. The maximum distance could be estimated by adopting the flow velocity as the primary's wind terminal speed (500 km s^{-1}), which amounts to 4–5 AU from the apex. However, the real distance should be much smaller than that, since close to the apex the winds collide almost radially. The high density at periastron leads to very fast cooling, so that the He II λ4686 line should be formed not very far from the WWC apex. Using the Hillier et al. (2001) model, we derive impact parameter of the primary's wind in the broadband B filter (which encompasses the He II λ4686 line) as $D_B = 4.4$ AU. Since the He II λ4686 emitting region is close to the WWC apex, which is very close to the primary star at periastron it could be eclipsed by the wind of the primary star for an intermediate orbital inclination. The expected duration of the eclipse of the He II λ4686 emitting region by the primary's stellar wind would be shorter than the X-ray emitting region, as the former is larger than the latter. In fact, the 2009.0 minimum in He II λ4686 lasted for a week as compared to the 4 weeks for the X-ray minimum. Both minima were centered at $\phi = 0.005$, reinforcing the nature of the He II λ4686 and the X-ray minima as due to occultation.

Soon after the minimum, the He II λ4686 starts rising again, reaching a local maximum (P3) in the phase range $\Delta\phi = 0.01$–0.03 (a duration of 40 days). Interestingly, the 2–10 keV X-ray emission increased very slowly at that time interval. We interpret this as a collapse of the WWC shock into deeper regions of the secondary stellar wind, where it is still being accelerated. As discussed by Parkin et al. (2009), Corcoran et al. (2010), and Parkin et al. (2011), radiative inhibition of the secondary's wind might lead to a collapse of the WWC onto the "surface" of the secondary when stars approach periastron. Of course, since the secondary star has a strong wind, it is likely that the momentum balance occurs at a radius larger than its photosphere. Accretion onto the companion star might also play a role (Soker & Behar 2006; Soker 2007), but is not a necessary condition to describe the observed phenomena. Thus, the secondary's wind is dominated by the radiation from the primary star (radiative inhibition) for a brief period and the hard X-ray source near the WWC apex is switched off. The associated
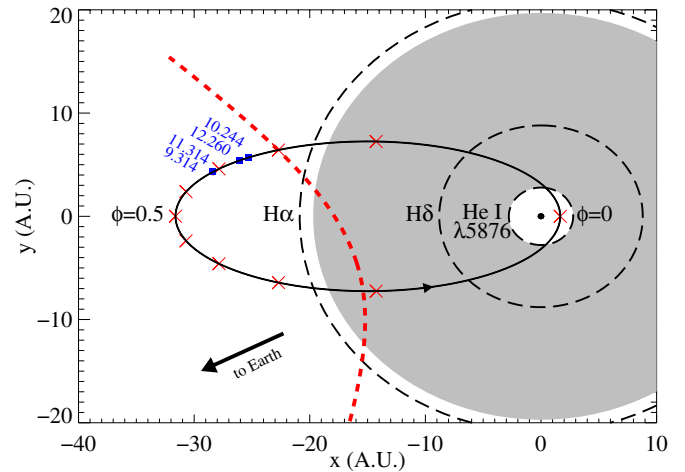
He II λ4686 emission may be absent during this time until the WWC forms anew. In the collapsed state, the WWC shock cone should be narrower, but still a powerful source at extreme UV energies, since the stellar winds continue to collide downstream of the stagnation point.

As the stars separate after periastron passage, there should be a point in the orbit when the winds collide at their full terminal speeds once again. At that time, the WWC shock would be restored, and consequently the hard X-rays emission would restart. However, the wind of the secondary needs to do extra work to push back the primary's wind. This is probably not a smooth process, because the momentum equilibrium in the WWC apex does not only depend on the global properties of the winds, but also on local properties: clumps driven by radiative instabilities in the primary wind (Moffat & Corcoran 2009) might produce stochastic variability as the wind–wind shock front tries to reform. Changes in the clump properties could in principle explain why the minimum in X-rays was much shorter in cycle 12 than in cycles 11 and 10, without needing to invoke a decrease by a factor of two in the mass-loss rate of the primary star (Corcoran et al. 2010). Also, lines formed deep in the primary's wind do not show particular changes in cycle 12 compared to earlier cycles. Figure 9 displays line profiles of the line Hδ taken almost at the same orbital phase ($\phi \sim 0.3$) along the last four cycles (data obtained with FEROS/ESO and OPD/Laboratório Nacional de Astrofísica). There are only small-scale variations in the P Cygni absorption strength and terminal speed. This line is relevant, since it is formed in regions of the primary's wind little affected by the WWC shock in the interval $\Delta\phi = 0.2$–0.8, as can be seen in Figure 10 (which is based on the model by Hillier et al. 2001). In this figure, the circles indicate the radii of maximum emissivity for different spectral lines. We also indicate the zone inside which the Hδ emissivity is larger than 50% of the peak intensity (dotted circle). Hα is affected by the WWC for most of the orbit and Fe II lines, formed at much larger distances from the central

13

star,[26] are disturbed by the WWC even at apastron. In this way, changes reported by Mehner et al. (2010b) in those lines cannot be attributed to the global properties of the primary's wind, but are probably driven by fluctuations in the WWC.

6. CONCLUSIONS

In this paper, we present data from the last four low-excitation events in η Car in the light of the He II $\lambda4686$ emission line. We summarize our results and conclusions below.

1. The He II $\lambda4686$ line is present at a faint level along most of the 5.538 yr cycle.
2. Two months before periastron, the He II $\lambda4686$ line strength increases dramatically with large flare-like oscillations on a timescale of weeks, similar to the X-ray "flares" seen just prior to periastron passage.
3. In the 2009.0 event, just before the minimum, there were two distinct peaks (P1 and P2) in the line equivalent width. Peaks P1 and P2 are correlated with flares seen in the X-rays light curve, after shifting the later by +16.5 days. They are not phase-locked and are probably due to localized density enhancements (clumps) in the primary's stellar wind.
4. There is an abrupt decrease in the line emission, reaching a minimum centered at $\phi = 0.005$. This minimum is centered at the same phase as the X-ray minimum, but lasts only a week. We argue that this minimum is an occultation of the He II $\lambda4686$ emitting region by the primary's stellar wind.
5. The fact that the disappearance of He II $\lambda4686$ emission in the central source and at the FOS4 position (in the SE lobe of the Homunculus) occurs close in time (but not simultaneously) is not an argument against an occultation, since the binary system revolves very quickly at periastron.
6. In the 2009.0 event, after the minimum, the He II $\lambda4686$ equivalent width shows another peak (P3), which appears to repeat from cycle to cycle. This peak is not correlated with the X-ray variation, as the He II $\lambda4686$ emission is in the high state when X-rays are very low. This He II $\lambda4686$ peak occurs in the phase range $\Delta\phi = 1.01$–1.035. Mehner et al. (2011) claim that P3 was present only in the 2009.0 event, suggesting this event to be different from previous ones. However, we have detected it clearly in 2009.0, 2003.5, and 1992.5 (see Figure 3) apparently with the same duration, although our poor time coverage during the past events prevented us from drawing any conclusion about the repeatability on the peak intensity. Our result is corroborated by Stahl et al. (2005) in their Figure 16, which also indicated a rise in He II $\lambda4686$ intensity after the 2003.5 minimum.
7. A potential mechanism to explain the P3 peak is a collapse of the WWC onto the "surface" of the secondary star due to radiative inhibition of the secondary's wind by photons from the primary star, which could shift most of the energy of the shocked gas to lower energies near the He$^+$ ionization threshold.
8. If the collapse scenario is valid, periastron occurs at $\phi \sim 0.02$ or a little earlier.
9. The He II $\lambda4686$ equivalent width did not display the early recovery seen in X-rays after the 2009.0 event. We suggest that the recovery of the WWC region from the collapse phase is driven by localized instabilities/clumps

---

[26] For example, the Fe II $\lambda4923$ emissivity is larger than 50% of the peak emissivity within a ring which goes from $\sim$25 to 140 AU from the primary star.

in the primary's wind as suggested by Akashi et al. (2006). Moffat & Corcoran (2009) suggested that clumps might explain flares in the X-ray light curve, and might control the momentum balance at scales on the clump size ($\sim$1 AU).

REFERENCES

Abraham, Z., & Falceta-Gonçalves, D. 2007, MNRAS, 378, 309
Abraham, Z., Falceta-Gonçalves, D., Dominici, T., Caproni, A., & Jatenco-Pereira, V. 2005, MNRAS, 364, 922
Akashi, M., Soker, N., & Behar, E. 2006, ApJ, 644, 451
Bartzakos, P., Moffat, A. F. J., & Niemela, V. S. 2001, MNRAS, 324, 33
Breysacher, J., & François, P. 2000, A&A, 361, 231
Cardelli, J. A., Clayton, G. C., & Mathis, J. S. 1989, ApJ, 345, 245
Corcoran, M. F. 2005, AJ, 129, 2018
Corcoran, M. F., Hamaguchi, K., Pittard, J. M., et al. 2010, ApJ, 725, 1528
Corcoran, M. F., Pollock, A. M. T., Hamaguchi, K., & Russell, C. 2011, in Proc. Stellar Winds in Interaction, ed. T. Eversberg & J. H. Knapen (arXiv:1101.1422)
Damineli, A. 1996, ApJ, 460, L49
Damineli, A. 1997, in ASP Conf. Ser. 120, Luminous Blue Variables: Massive Stars in Transition, ed. A. Nota & H. Lamers (San Francisco, CA: ASP), 272
Damineli, A., Conti, P. S., & Lopes, D. F. 1997, New Astron., 2, 107
Damineli, A., Hillier, D. J., Corcoran, M. F., et al. 2008a, MNRAS, 386, 2330
Damineli, A., Hillier, D. J., Corcoran, M. F., et al. 2008b, MNRAS, 384, 1649
Damineli, A., Kaufer, A., Wolf, B., et al. 2000, ApJ, 528, L101
Damineli, A., Lopes, D. F., & Conti, P. S. 1999, in ASP Conf. Ser. 179, Eta Carinae At The Millennium, ed. J. A. Morse, R. M. Humphreys, & A. Damineli (San Francisco, CA: ASP), 288
Damineli, A., Stahl, O., Kaufer, A., et al. 1998, A&AS, 133, 299
Davidson, K., Ebbets, D., Johansson, S., Morse, J. A., & Hamann, F. W. 1997, AJ, 113, 335
Davidson, K., Ebbets, D., Weigelt, G., et al. 1995, AJ, 109, 1784
Davidson, K., Martin, J., Humphreys, R. M., et al. 2005, AJ, 129, 900
de la Chevrotière, A., Moffat, A. F. J., & Chené, A. N. 2011, MNRAS, 411, 635
Dorland, B. N., Currie, D. G., & Hajian, A. R. 2004, AJ, 127, 1052
Fahed, R., Moffat, A. F. J., Zorec, J., et al. 2011, Soc. R. Sci. Liège, 80, 668
Falceta-Gonçalves, D., & Abraham, Z. 2009, MNRAS, 399, 1441
Ferland, G. J., Korista, K. T., Verner, D. A., et al. 1998, PASP, 110, 761
Fernandez Lajus, E., Farina, C., Calderon, J. P., et al. 2010, New Astron., 15, 108
Fernandez Lajus, E., Farina, C., Torres, A. F., et al. 2009, A&A, 493, 1093
Flores, A., Auer, L. H., Koenigsberger, G., & Cardona, O. 2001, ApJ, 563, 341
Gaviola, E. 1953, ApJ, 118, 234
Groh, J. H., & Damineli, A. 2004, Inf. Bull. Var. Stars, 5492, 1
Groh, J. H., Nielsen, K. E., Damineli, A., et al. 2010, A&A, 517, 9
Gull, T. R., Madura, T. I., Groh, J. H., & Corcoran, M. F. 2011, ApJ, 743, L3
Gull, T. R., Nielsen, K. E., Corcoran, M. F., et al. 2009, MNRAS, 396, 1308
Hamaguchi, K., Corcoran, M. F., Gull, T., et al. 2007, ApJ, 663, 522
Henley, D. B., Corcoran, M. F., Pittard, J. M., et al. 2008, ApJ, 680, 705

Hill, G. M., Moffat, A. F. J., & St-Louis, N. 2002, MNRAS, 335, 1069
Hillier, D. J., Davidson, K., Ishibashi, K., & Gull, T. R. 2001, ApJ, 553, 837
Hillier, D. J., Gull, T., Nielsen, K., et al. 2006, ApJ, 642, 1098
Hubrig, S., Briquet, M., Morel, T., et al. 2008, A&A, 488, 287
Ishibashi, K., Corcoran, M. F., Davidson, K., et al. 1999, ApJ, 524, 983
Kashi, A., & Soker, N. 2008, MNRAS, 390, 1751
Kaufer, A., Stahl, O., Tubbesing, S., et al. 1999, Messenger, 95, 8
Koenigsberger, G., Georgiev, L., Hillier, D. J., et al. 2010, AJ, 139, 2600
Madura, T. I., Gull, T. R., Owocki, S. P., et al. 2011, MNRAS, in press (arXiv:1111.2226)
Marchenko, S. V., Moffat, A. F. J., Ballereau, D., et al. 2003, ApJ, 596, 1295
Marchenko, S. V., Moffat, A. F. J., Eenens, P. R. J., et al. 1997, ApJ, 485, 826
Martin, J. C., Davidson, K., Humphreys, R. M., Hillier, D. J., & Ishibashi, K. 2006, ApJ, 640, 474
McGregor, P. J., Rathborne, J. M., & Humphreys, R. M. 1999, in ASP Conf. Ser. 179, Eta Carinae At The Millennium, ed. J. A. Morse, R. M. Humphreys, & A. Damineli (San Francisco, CA: ASP), 236
Mehner, A., Davidson, K., Ferland, G. J., & Humphreys, R. M. 2010a, ApJ, 710, 729
Mehner, A., Davidson, K., Humphreys, R. M., et al. 2010b, ApJ, 717, L22
Mehner, A., Davidson, K., Martin, J. C., et al. 2011, ApJ, 740, 80
Moffat, A. F. J., & Corcoran, M. F. 2009, ApJ, 707, 693
Moffat, A. F. J., Marchenko, S. V., Bartzakos, P., et al. 1998, ApJ, 497, 896
Nazé, Y., & Rauw, G. 2008, A&A, 490, 801
Okazaki, A. T., Owocki, S. P., Russell, C. M. P., & Corcoran, M. F. 2008, MNRAS, 388, L39
Paczynski, B. 1998, ApJS, 494, L45
Parkin, E. R., Pittard, J. M., Corcoran, M. F., & Hamaguchi, K. 2011, ApJ, 726, 105
Parkin, E. R., Pittard, J. M., Corcoran, M. F., Hamaguchi, K., & Stevens, I. R. 2009, MNRAS, 394, 1758
Pittard, J. M., & Corcoran, M. F. 2002, A&A, 383, 636
Rodgers, A. W., & Searle, L. 1967, MNRAS, 135, 99

Schnurr, O., Moffat, A. F. J., Villar Sbaffi, A., St-Louis, N., & Morrell, N. I. 2009, MNRAS, 395, 823
Smith, N., & Frew, D. J. 2011, MNRAS, 415, 2009
Smith, N., Li, W., Foley, R. J., et al. 2007, ApJ, 666, 1116
Smith, N., Morse, J. A., Gull, T. R., et al. 2004, ApJ, 605, 405
Soker, N. 2003, ApJ, 597, 513
Soker, N. 2005, ApJ, 635, 540
Soker, N. 2007, ApJ, 661, 482
Soker, N., & Behar, E. 2006, ApJ, 652, 1563
Sota, A., Maíz Apellániz, J., Walborn, N. R., et al. 2011, ApJS, 193, 24
Stahl, O., Weis, K., Bomans, D. J., et al. 2005, A&A, 435, 303
Steiner, J. E., & Damineli, A. 2004, ApJ, 612, L133
Teodoro, M., Damineli, A., Sharp, R. G., Groh, J. H., & Barbosa, C. L. 2008, MNRAS, 387, 564
Thackeray, A. D. 1953, MNRAS, 113, 211
Thackeray, A. D. 1967, MNRAS, 135, 51
Tody, D. 1993, in ASP Conf. Ser. 52, Astronomical Data Analysis Software and Systems II, ed. R. J. Hanisch, R. J. V. Brissenden, & J. Barnes (San Francisco, CA: ASP), 173
Usov, V. V. 1992, ApJS, 389, 635
van Genderen, A. M., Sterken, C., Allen, W. H., & Walker, W. S. G. 2006, J. Astron. Data, 12, 3
Verner, E., Bruhweiler, F., & Gull, T. 2005, ApJ, 624, 973
Walborn, N. R., Sota, A., Maíz Apellániz, J., et al. 2010, ApJS, 711, L143
Weigelt, G., Albrecht, R., Barbieri, C., et al. 1995, RevMexAA Ser. Conf., 2, 11
Weigelt, G., & Ebersberger, J. 1986, A&A, 163, L5
White, R. L., & Becker, R. H. 1995, ApJ, 451, 352
Whitelock, P. A., Feast, M. W., Koen, C., Roberts, G., & Carter, B. S. 1994, MNRAS, 270, 364
Williams, P. 2011, Bull. Soc. R. Sci. Liege, 80, 595
Williams, P. M., van der Hucht, K. A., Pollock, A. M. T., et al. 1990, MNRAS, 243, 662
Zanella, R., Wolf, B., & Stahl, O. 1984, A&A, 137, 79